

Article

Applications of Oxyhydrogen, Direct Water Injection, and Early-Intake Valve Closure Technologies on a Petrol Spark Ignition Engine—A Path towards Zero-Emission Hydrogen Internal Combustion Engines

Xiangtao Kong and Yaodong Wang * 

Engineering Department, Durham University, Durham DH1 3LE, UK; xiangtao.kong@durham.ac.uk

* Correspondence: yaodong.wang@durham.ac.uk; Tel.: +44-(0)-191-33-42377

Abstract: This study investigates the performance of a 4-MIX engine utilizing hydrogen combustion in pure oxygen, water injection, and the application of the early-intake valve closure (EIVC) Miller cycle. Transitioning from a standard petrol–oil mix to hydrogen fuel with pure oxygen combustion aims to reduce emissions. Performance comparisons between baseline and oxyhydrogen engines showed proportional growth in the energy input rate with increasing rotational speed. The oxyhydrogen engine exhibited smoother reductions in brake torque and thermal efficiency as rotational speed increased compared to the baseline, attributed to hydrogen’s higher heating value. Water injection targeted cylinder and exhaust temperature reduction while maintaining a consistent injected mass. The results indicated a threshold of around 2.5 kg/h for the optimal water injection rate, beyond which positive effects on engine performance emerged. Investigation into the EIVC Miller cycle revealed improvements in brake torque, thermal efficiency, and brake specific fuel consumption as early-intake valve closure increased. Overall, the EIVC model exhibited superior energy efficiency, torque output, and thermal efficiency compared to alternative models, effectively addressing emissions and cylinder temperature concerns.

Keywords: oxyhydrogen combustion; direct water injection; EIVC; petrol SI engine



Citation: Kong, X.; Wang, Y. Applications of Oxyhydrogen, Direct Water Injection, and Early-Intake Valve Closure Technologies on a Petrol Spark Ignition Engine—A Path towards Zero-Emission Hydrogen Internal Combustion Engines. *Energies* **2024**, *17*, 2014. <https://doi.org/10.3390/en17092014>

Academic Editor: Jiro Senda

Received: 6 February 2024

Revised: 2 April 2024

Accepted: 13 April 2024

Published: 24 April 2024



Copyright: © 2024 by the authors. Licensee MDPI, Basel, Switzerland. This article is an open access article distributed under the terms and conditions of the Creative Commons Attribution (CC BY) license (<https://creativecommons.org/licenses/by/4.0/>).

1. Introduction

Energy requirements have become one of the most concerning problems for the global environment nowadays [1]. The total amount of energy consumed by the global market increased from 396.0 exajoules in 2000 to 604 exajoules in 2022, with the majority of energy consumed by non-OECD countries. It was reported that global energy consumption for all non-OECD countries increased by 2.4% from 2011 to 2021. Conversely, for OECD and EU countries, energy consumption decreased slightly by 0.2% and 0.6%, respectively. Encouragingly, the share of oil consumption worldwide dropped from 39% in 2000 to 31% in 2021, while the share of renewable energy consumption increased from nearly 0% in 2000 to 7% in 2021 [2].

Another problem triggered by increasing energy demand is the surge of unwanted emissions including carbon, nitrogen, and sulphur oxides [3]. Since the Paris Agreement [4] had been claimed to restrict carbon emission in 2015, the carbon dioxide emissions only increased by 0.6% from 2011 to 2021 [2]. But as for NO_x emissions, the data provided by the World Bank showed that they increased from 2.72 trillion tons in 2010 to 3.02 trillion tons in 2020 [5]. Such a surge (>10% increase rate in 10 years) of NO_x emissions has attracted some researchers’ attention. Until 2023, the research on NO_x emission reduction techniques has become one of the most popular research topics in the field of engine technologies.

Concerning internal combustion engine (ICE) technologies, the two most common types of engines modifiable for renewable energy usage are spark ignition (SI) and compression ignition (CI) internal combustion engines (ICEs). They differ in approaches of

ignition and fuel supply. The SI engine is a type of engine in which the combustion process is triggered by a spark generated by a spark plug. And there is usually a carburetor attached to the SI ICE's intake, which improves the even mixing of air and fuel before injection. The port fuel injection method is usually used for SI ICEs due to the requirements of smooth flame build-up and stable air–fuel mixing. This technique is the injection of an air–fuel mixture into the intake manifold rather than directly into the combustion chamber (direct injection technique). Spark ignition internal combustion engines commonly work on original or modified Otto cycles [6]. And as for CI ICEs, the combustion process is triggered by the heat of the compressed air. Compression ignition engines commonly work on diesel or modified diesel cycles. During the intake stroke, only air or other kinds of carrier fluid inducted into the combustion chamber and the fuel will then be directly injected into the combustion chamber for compression ignition. Compression ignition internal combustion engines have higher compression ratios, which thus result in higher thermal efficiency and power output. But on the other hand, CI ICEs' combustion progress is less even than that of SI ICEs, so the emissions of unburned hydrocarbons are higher if fossil fuels are used [7].

The principle of hydrogen-fueled internal combustion engines dates back to the 1970s [8], with the first H₂-ICE prototype designed and built by Sir Francois Isaac de Rivaz of Switzerland in 1806 [9]. The Miller cycle, proposed by Ralph Miller in 1957 [10], involves adjustments to intake valve lift and timing profiles to isolate the compression stroke from the expansion stroke [11], improving efficiency, reducing emissions, and enhancing power output, especially at high rotational speeds [12]. However, hydrogen's properties of low ignition energy and low density pose potential hazards of abnormal combustion, including pre-ignition, backfire, knock, and spontaneous ignition [12].

Water injection techniques, known for their effectiveness in improving engine performance and preventing knock [13], have been utilized since World War I and were further developed during World War II, mainly for high-output aircraft engines. Research by P. Xu et al. [14,15] investigated the combustion and emission characteristics of a hydrogen-fueled spark ignition engine with direct water injection, showing significant reductions in NO_x emissions with increased water injection.

Lean-burn combustion, especially for spark ignition engines, has garnered significant research attention due to its potential to reduce negative pumping work and improve cycle efficiency. However, lean-burn combustion may increase NO_x formation due to higher air intake.

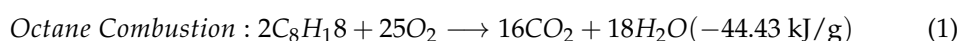
Research by Z. Ran et al. studied the lean spark ignition combustion of various fuels, highlighting syngas's stability under extremely lean conditions and its low lean misfire limit [16]. Simulation studies by Li [17] using a 1D Navier–Stokes equation solver and Realis WAVE software developed a dual-piston, two-stroke spark ignition engine with green fuel replacement and intake valve closure principles.

This study introduces an oxyhydrogen ICE model with direct water injection and early-intake valve closure (EIVC) technologies developed using Realis WAVE software. While some research exists on hydrogen applications in IC engines, few studies focus on oxyhydrogen combustion combined with water injection and the Miller cycle. The aim of this research is to conduct a simulation study in this area and investigate engine performance. The baseline model was validated and then modified into an oxyhydrogen-powered engine to eliminate emissions. Water injection was then applied to reduce the cylinder temperature and increase the gas mass within the cylinder. EIVC technology was also integrated for further improvements, resulting in an H₂-O₂-H₂O ICE model capable of zero-emission exhaust and slightly better performance than the original gasoline-fueled engine.

2. Theory and Methods

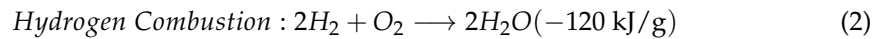
2.1. Fuel Combustion Theory

The chemical reaction equation for the combustion of octane is shown in Equation (1):



where -44.43 kJ/g is the enthalpy change as well as the heating value of octane. Octane is the main component of petrol.

The chemical reaction equation for the formation of water by oxyhydrogen combustion is shown in Equation (2):



where -120 kJ/g is the heating value of hydrogen, which is nearly three times as large as octane.

2.2. Miller Cycle Theory

Ralph Miller proposed two variations for the intake valve closure concept: early-intake valve closure (EIVC) and late-intake valve closure (LIVC) [18]. There is also another approach called the early rotary-valve closure (ERVC) that requires the attachment of a rotating valve between the intake pipe and intake valve [19]. In this study, only the early-intake valve closure technique was applied. Figure 1 shows the principle of early-intake valve closure in terms of the P-V diagram.

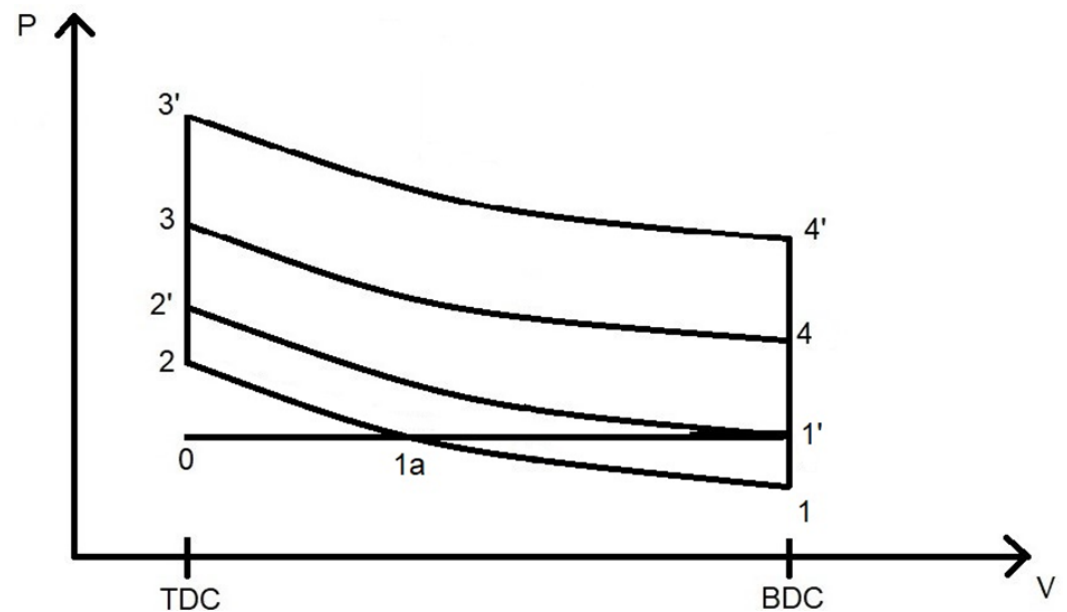


Figure 1. P-V diagram of the Otto and EIVC Miller cycle.

The cycle $0-1'-2'-3'-4'-1'-0$ shows the P-V relationship of a standard Otto cycle, and the cycle $0-1a-1-2-3-4-1-1a-0$ shows the P-V relationship of an EIVC Miller cycle. The intake valve opens at point 0 and closes at point 1a. In EIVC Miller cycles, the intake valve remains open for a shorter period of time. Stage $1-1a$ in Figure 1 shows the blow-back effect produced by the EIVC. After the intake valve closes at 1a, the downward movement of the piston decreases the cylinder pressure from ambient at stage 1a until stage 1, when the piston reaches the bottom of the combustion chamber. The sub-ambient pressure inside the combustion chamber between stage 1a and 1 produces the so-called 'blow-back' effect, which consumes only a negligible amount of energy to bring the piston from the bottom position back to the position when the intake valve was closed; then, the compression stroke starts. The EIVC shortens the compression stroke while keeping the expansion stroke, thus increasing the overall engine efficiency.

There are two different approaches to implementing EIVC with the same principle: variable valve timing (VVT) and variable valve lift (VVL) [20,21]. VVT adjusts the duration of valve opening, while VVL modifies the valve lift values to reduce the rate of gas intake and enhance the blow-back effect. In this study, both techniques were applied

and expected to significantly enhance the effects of EIVC. The specific procedures are outlined in Section 2.5.

Typically, Miller cycle ICEs are equipped with a supercharger or turbocharger to offset the effect of induced air loss caused by EIVC. However, since this study utilizes the lean burn technique and proportional injectors, the induction loss from EIVC can be ignored. Therefore, neither a supercharger nor a turbocharger was included in the model's structure.

2.3. Baseline Model Structure Development Method

The baseline model was developed based on the experimental data provided in the study by Knaus et al. [22] for a 31 cc version of the Stihl 4-MIX engine design, as shown in Figure 2. After validating the baseline model, additional upgrades were implemented to improve its emission characteristics while maintaining performance integrity. The refined model's structure is depicted in Figure 3, with modifications primarily concentrating on parameters. The only structural discrepancy between the two models is the inclusion of a water mass flow injector, labeled `Injector_H2O`.

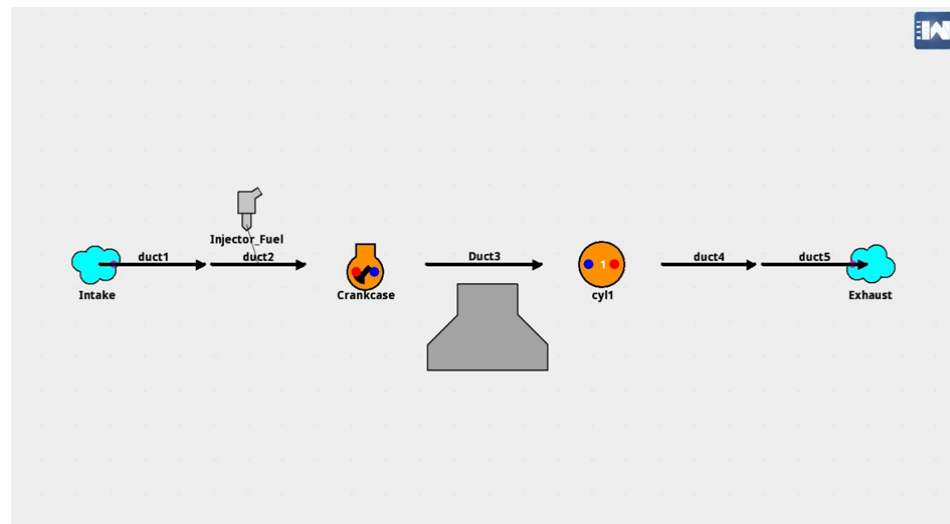


Figure 2. Baseline model.

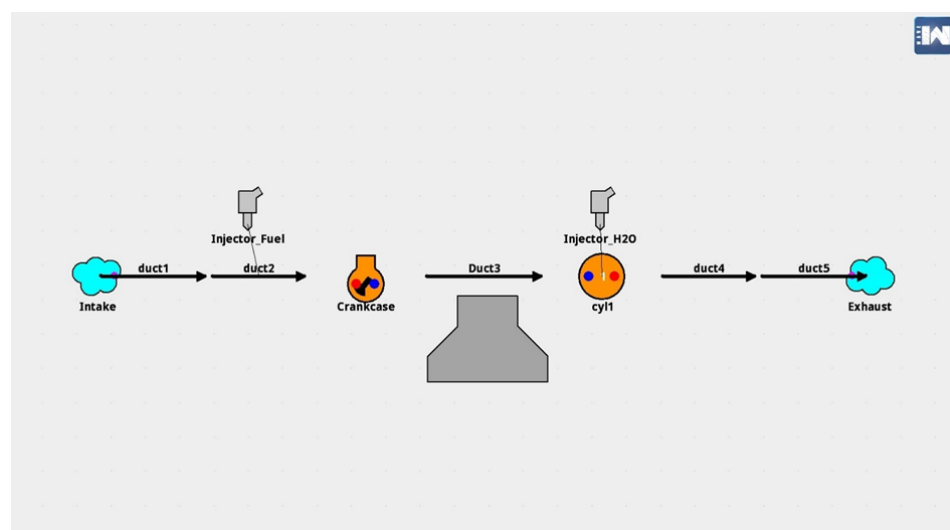


Figure 3. Upgraded model.

The main structure of the ultimate upgraded model is shown in Figure 3. The elements are shown and explained in the list below:

- Ambient elements, including the intake and the exhaust. Ambient elements are sources and ends of flows. They were both set as the ordinary atmospheric conditions;
- Duct elements, including ducts 1–5. Ducts 1 and 2 are different sections of the intake duct. Duct 3 is the route between the crankcase and cylinder. Ducts 4 and 5 are different sections of the exhaust duct, which leads to the exhaust;
- Crankcase element, representing the crankcase of a piston engine cylinder. It can only be used for ICEs and is commonly used in two-stroke engines. In this report, the crankcase element was used in a four-stroke engine model and set up in the engine block element. It can be used to study the engine's pumping work;
- Engine block element, which is the grey volcano-shaped element under the element Duct 3. It was used to control and set up some key parameters of the model including engine speed, engine friction model, engine type, number of engine strokes, and the emission model;
- Cylinder element, labelled *cy11*, is used to model the cycle progress of a cylinder. It can be used to control the geometry, combustion submodels, and the heat transfer submodel.
- Injector elements, including the fuel injector in the baseline model (labelled *Injector_Fuel*) and the water injector in the upgraded model (labelled *Injector_H2O*). The fuel injector element was set as a proportional injector, which means the ratio between fuel and air is always constant. The water injector in the upgraded model (labelled *Injector_H2O*) was set as a mass flow rate injector, which takes control of the injection rate and injection pressure.

Specific settings are shown in Appendixes B–N.

2.4. Submodel Modification Method

There are three essential submodels modified in this study: the Chen–Flynn friction model, the Woschini heat transfer model, and the multi-Wiebe combustion model [23].

2.4.1. Chen–Flynn Friction Model

The Chen–Flynn Friction Model in Realis WAVE utilises the Chen–Flynn correlation to achieve solid friction predictions. The complete equation is shown in Equation (3).

$$FMEP = A_{cf} + \frac{1}{ncyl} \sum_{i=1}^{ncyl} [B_{cf}(P_{max})_i + C_{cf} * (S_{fact})_i + Q_{cf} * (S_{fact})_i^2] \quad (3)$$

with

$$S_{fact} = RPM * stroke / 2 \quad (4)$$

where A_{cf} , B_{cf} , C_{cf} , and D_{cf} are user-defined variables.

The parameter A_{cf} is a constant that shall be entered directly by users, it influences simulation results the most effectively. The parameter B_{cf} shows a linear relationship to peak cylinder pressure. The parameter C_{cf} shows a linear relationship to the piston speed. And parameter D_{cf} shows a quadratic relationship to the piston speed [23].

2.4.2. Woschni Heat Transfer Model

An assumption was made within the Woschni heat transfer model of Realis WAVE that it deems the charge to have a uniform distribution of heat flow coefficient and velocity on all surfaces. Then it calculates the amount of heat transferred to and away from the charge.

The equation of the Woschni heat transfer model is shown in Equation (5).

$$h_g = 0.0128 D^{-0.20} P^{0.80} T - 0.53 v_c^{0.80} C_{enht} \quad (5)$$

where D is the length of the cylinder bore, p is the cylinder pressure, T is the cylinder temperature, v_c is the characteristic velocity, C_{enht} is the user-entered multiplier and set as 1, which is the default value set by Realis WAVE.

The characteristic velocity is defined in Equation (6).

$$v_c = c_1 v_m + c_2 \frac{V_D T_r}{P_r V_r} (P - P_{mot}) \quad (6)$$

where v_m is the mean piston speed, V_D is the cylinder displacement, T_r is the reference temperature (values right after intake valve closing), P_r is the reference pressure (values right after intake valve closing), V_r is the reference volume, P_{mot} is the motored cylinder pressure, and c_1 and c_2 are given constants.

In this study, the original Woschni model was used, and both the heat transfer coefficients were set to 1 as default values.

2.4.3. Multi-Wiebe Combustion Model

Regarding the combustion submodel, this study employed the multi-Wiebe combustion model and incorporated water injection. Realis WAVE considers water as a type of fuel in its calculations, necessitating the use of the multi-Wiebe combustion model instead of the single SI Wiebe combustion model. This model is capable of handling calculations involving multiple types of fuels in combustion, allowing for the combination of more than one SI Wiebe combustion burn rate curve if required. However, despite utilizing the multi-Wiebe combustion model, only one burn rate curve was applied to both fuels (the main fuel and water). This is due to the unique non-combustible characteristic of water compared to all other burnable fuels in Realis WAVE simulations. The equation for multi-Wiebe combustion is presented in Equation (7).

$$W = \sum_n *W_n \quad (7)$$

where W is the sum of all single curves' results. W_n is the non-dimensional burn rate for a single curve. The equation for calculating the single burn rate curve W_n is shown in Equation (8).

$$W_n = 1 - \exp[-a(\theta_i - \theta_0)^{b+1}] \quad (8)$$

where a , b are unitless factors and $\theta_i - \theta_0$ is the combustion duration; it is 42 CAD in this study. Realis WAVE utilises these three factors and the one-point curve approach to automatically form the complete multi-Wiebe combustion curve. The combined curve is shown in Figure 4.

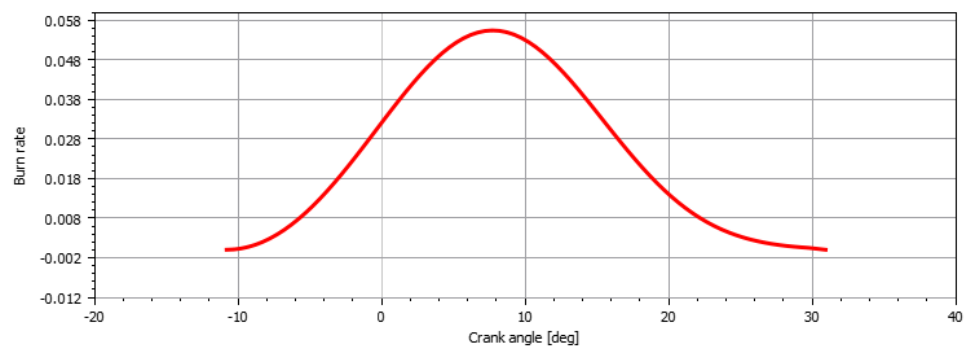
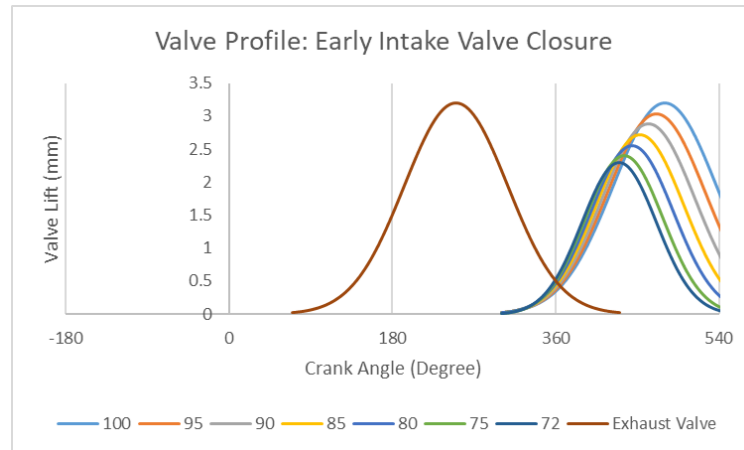


Figure 4. Parameters of the multi-Wiebe combustion model.

The burn fraction at completion was set as 0.96 because there was 4% unburned fuel as a part of the exhaust gas.

2.5. Valve Opening Profile Modification Method

There are mainly two variations of intake valve closure: early-intake valve closure (EIVC) and late-intake valve closure (LIVC). In this report, only the EIVC technique was implemented. Valve lift and timing profiles are shown in Figure 5. The exact method of calculation is shown in Appendix A.



(a)

Valve Open Percentage (%)	Open Duration (CAD)	Max. Valve Lift (mm)
100	360	3.20
95	345	3.04
90	327	2.88
85	309	2.72
80	291	2.56
75	273	2.40
72	259	2.30

(b)

Figure 5. Variable valve lifts and timings: (a) line chart. (b) Table with exact open durations and lifts.

2.6. Water Injection Rate Calculation Method

According to the mass flow rate equation of total injected mass,

$$\dot{m}_{total} = \dot{m}_{fuel} + \dot{m}_{air} \quad (9)$$

The total injected mass of the 4-MIX engine is

$$\dot{m}_{total} = \dot{m}_{petrol} + \dot{m}_{air} = 0.496 \text{ kg/h} + 5.956 \text{ kg/h} = 6.453 \text{ kg/h} \quad (10)$$

Under the stoichiometric condition, while keeping the energy input rate constant at 5.51 kW, 0.169 kg/h of hydrogen was required. Thus,

$$\dot{m}_{H_2} = 0.169 \text{ kg/h} \quad (11)$$

According to the moles equation of water formation:



$$4 + 32 = 36 \quad (13)$$

The mass flow rate of pure oxygen required for all hydrogen to be burned is

$$\dot{m}_{O_2} = \dot{m}_{H_2} * 8 = 1.352 \text{ kg/h} \quad (14)$$

Under the actual Realis WAVE simulation environment, while keeping the energy input rate constant at 5.51 kW, 0.169 kg/h of hydrogen was required as the fuel. Due to the limitation of the proportional injector element, the requirements of pure oxygen were as high as 3.144 kg/h, as a compulsory lean-burn condition. This value was automatically determined by Realis WAVE's proportional injector model. On the other hand, this compulsory lean

burn offsets the loss caused by EIVC or even enhances it further. Thus, the mass flow rate of water required for keeping the mass constant is

$$\dot{m}_{H_2O} = \dot{m}_{total} - \dot{m}_{O_2} \quad (15)$$

$$\dot{m}_{H_2O} = 6.453 \text{ kg/h} - 0.169 \text{ kg/h} - 3.144 \text{ kg/h} = 3.14 \text{ kg/h} \quad (16)$$

Simulations were carried out with a water injection rate up to 2 times as obtained for further analysis. Specific processes and results are shown in Section 3.3.

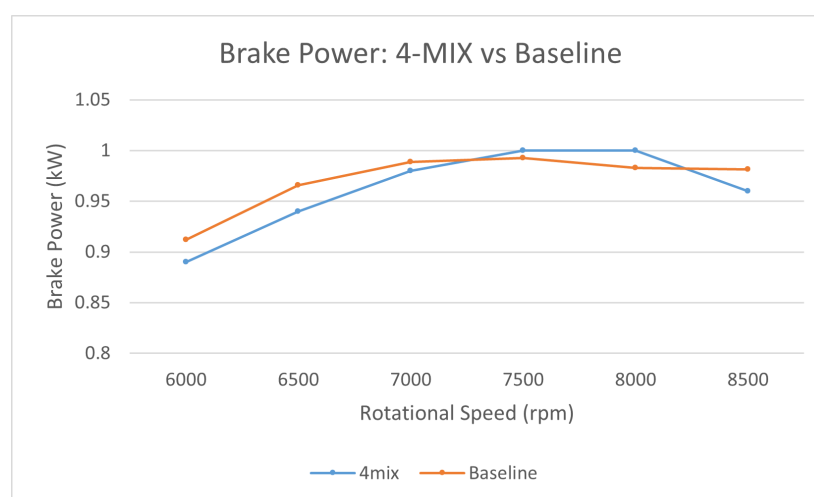
3. Results and Discussion

The simulation results are organized, documented, and discussed in this section. Three models were developed in total. Initially, a baseline model was created and meticulously calibrated for accuracy. Subsequent progressive upgrades were implemented, each aimed at enhancing performance based on the analysed results obtained at each stage. Ultimately, the final model exhibited superior performance and emission characteristics compared to all other models.

3.1. Baseline Model

3.1.1. Brake Power Validation

Figure 6 shows the comparisons between the original 4-MIX engine experimental results and the baseline model's simulated brake power with the increment of rotational speed. Specific results and errors are shown in Figure 6b.



(a)

Rotational Speed (rpm)	4-MIX Brake Power (kW)	Baseline Brake Power (kW)	Error (%)
6000	0.890	0.912	2.50
6500	0.940	0.966	2.74
7000	0.980	0.989	0.89
7500	1.000	0.933	-0.71
8000	1.000	0.983	-1.71
8500	0.960	0.981	2.23

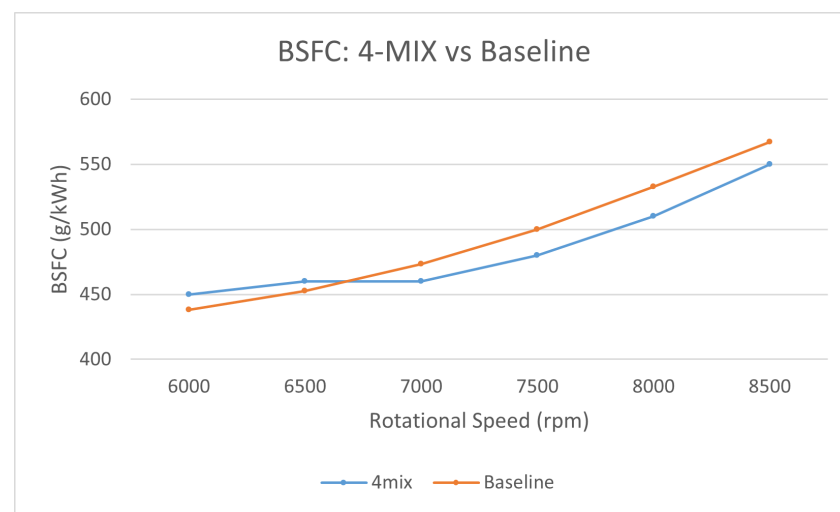
(b)

Figure 6. Baseline model validation: brake power. (a) Line chart. (b) Table with percentage errors.

After conducting comparisons, it was ensured that all predicted brake power errors remained below 5% across all rotational speeds. Both sets of results reached their peaks at a rotational speed of 7500 rpm, precisely matching the rated speed of the 4-MIX engine. This demonstrates that the simulation model closely aligns with the operational principles of the original 4-MIX engine's simulation. Both the experimental and baseline model simulation data exhibit downward trends at higher speeds. Practically, this trend arises from the high demand but inadequate supply of air, specifically, oxygen for combustion, at high engine speeds. In the simulations, this was simulated by increasing the frictional force at high rotational speeds, as described in Section 2.4.1.

3.1.2. Brake Specific Fuel Consumption Validation

Figure 7 shows comparisons of brake specific fuel consumption (BSFC) between the 4-MIX engine and the baseline model with the increment of rotational speed. Specific results are tabulated in Figure 7b.



(a)

Rotational Speed (rpm)	4-MIX BSFC (kW)	Baseline BSFC (kW)	Error (%)
6000	450	438.20	-2.62
6500	460	452.54	-1.62
7000	460	473.25	2.88
7500	480	499.93	4.15
8000	510	532.93	4.46
8500	550	567.09	3.11

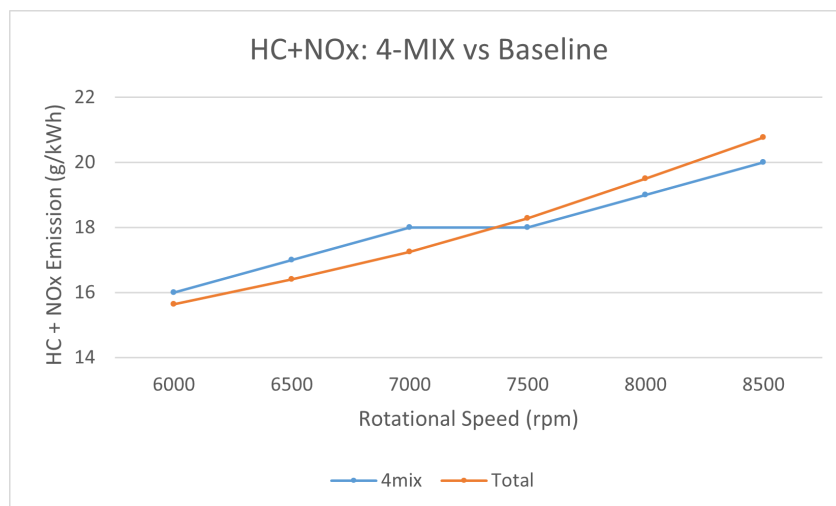
(b)

Figure 7. Baseline model validation: BSFC. (a) Line chart. (b) Table with percentage errors.

From Figure 7b, it can be seen that all errors were kept under 5% at all rotational speeds.

3.1.3. HC + NO_x Emission Validation

Figure 8 shows comparisons of combined unburned hydrocarbon and nitrogen oxides emission (HC + NO_x) between the 4-MIX engine and the baseline model. Specific results are listed in Figure 8b.



(a)

Rotational Speed (rpm)	4-MIX HC+NOx Emission (g/kWh)	Baseline HC Emission (g/kWh)	Baseline NOx Emission (g/kWh)	Baseline HC+NOx Emission (g/kWh)	Error (%)
6000	16	15.30	0.33	15.63	-2.29
6500	17	16.05	0.34	16.40	-3.54
7000	18	16.87	0.38	17.25	-4.19
7500	18	17.86	0.42	18.28	1.54
8000	19	19.03	0.47	19.50	2.61
8500	20	20.25	0.51	20.76	3.79

(b)

Figure 8. Baseline model validation: HC + NOx Emission. (a) Line chart. (b) Table with percentage errors.

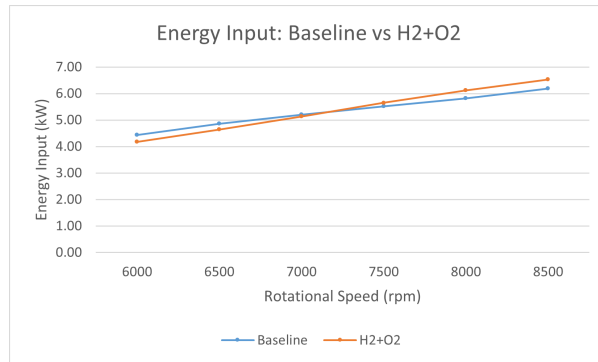
As it can be seen from Figure 8b, all errors are kept under 5% in all rotational speeds.

3.2. Hydrogen Combustion in Pure Oxygen

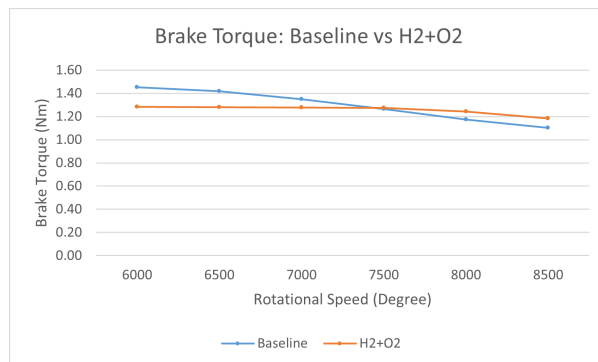
The original 4-MIX engine was fuelled with a standard petrol–oil mix (50:1). Utilising such a type of fossil fuel mixture and air as the oxidiser caused unwanted emissions, including nitrogen and carbon compounds. Both the fossil fuel mixture and the air are sources of those undesired elements. Thus, to ultimately eliminate them from emissions, principles of hydrogen fuel replacement and pure oxygen combustion were both applied to the baseline model. The upgraded model can therefore produce zero emissions, theoretically. Figure 9 presents the oxyhydrogen engine model's performance results at varying rotational speeds.

3.2.1. Baseline vs. Oxyhydrogen Models: Performance Comparisons

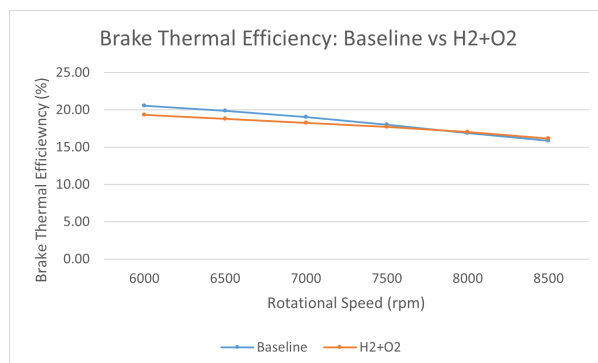
Figure 9a shows the energy input rate results of the baseline and oxyhydrogen models. Both of these lines are nearly straight, which show that the growth of energy input rate is proportional to the growth of rotational speed. Each 500 rpm increment of rotational speed can boost the increment of energy input for 0.5 kW. The energy input rate of these two models was controlled on a similar level (5.51 kW).



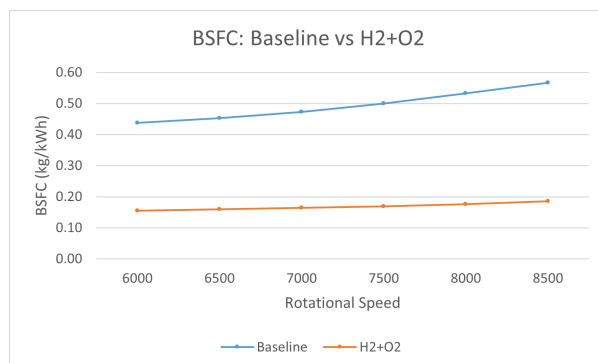
(a)



(b)



(c)



(d)

Figure 9. Baseline model vs. oxyhydrogen: engine performance comparisons. (a) Energy input, (b) brake power, (c) brake thermal efficiency, (d) brake specific fuel consumption.

Figure 9c shows the change in brake thermal efficiency versus the change in rotational speed for both the baseline and oxyhydrogen models. Both lines show downward trends with constant gradients. The thermal efficiency of the baseline model begins from 20.54% at a rotational speed of 6000 rpm and then starts to fall until reaching around 16% at a rotational speed of 8500 rpm. The thermal efficiency of the oxyhydrogen model shows a similar trend to the baseline model. It starts from 19.33% at a rotational speed of 8500 rpm, which is slightly lower than the thermal efficiency of the baseline model at that speed. After that, the line of the oxyhydrogen model begins to drop and eventually overlaps with the line of the baseline model at a rotational speed of 8500 rpm. Generally, the difference between the two curves keeps falling as the rotational speed increases and it reaches its lowest level at a rotational speed of 8500.

Figure 9d presents the brake specific fuel consumption of both models. Both of these curves present bend-up tendencies. This tendency can be explained according to the reduction in thermal efficiency. A lower efficiency caused more energy to be wasted; thus, a higher fuel consumption rate was obtained. It is very apparent that the BSFC of the oxyhydrogen model is generally three times as large as that of the baseline model. This interesting multiplicative relationship can be ascribed to the multiplicative relationship of petrol and hydrogen's heating value, as mentioned previously in Section 2.1. The percentage differences were huge between these two models, mostly higher than 65%.

Figure 9b presents the brake torque curves of the baseline and the oxyhydrogen model at varying CAD. Generally speaking, both curves present upward tendencies. This can be explained by the reduction in brake thermal efficiency shown in Figure 9c. However, the curve of the oxyhydrogen model decreases more gently; the increment of rotational speed at 2500 rpm only reduces the brake torque by 0.1 kW. At low and medium rotational speeds, the value of the oxyhydrogen model barely changes. And as for the brake torque of the baseline model, it falls as the rotational speed rises. Each addition of 500 rpm sees a reduction of 0.07 kW. The difference between the two curves is the largest when operating at a rotational speed of 6000 rpm and then decreases to nearly 0 at a rotational speed of 7500 rpm. After the rated rotational speed, the brake torque of the oxyhydrogen model eventually becomes higher than that of the baseline model.

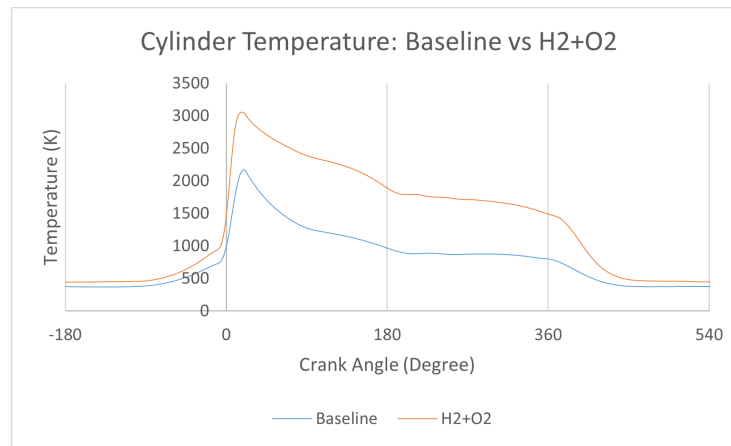
3.2.2. Baseline vs. Oxyhydrogen Models: Temperature and Pressure Comparisons

Figure 10 presents comparisons of cylinder temperature and cylinder pressure.

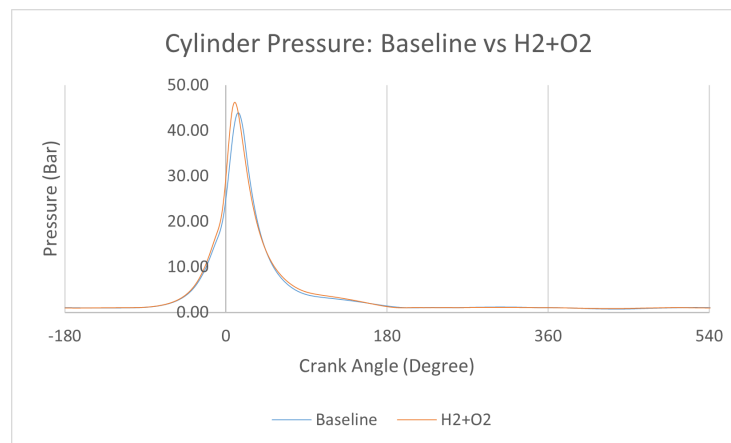
In Figure 10a, the cylinder temperature of the oxyhydrogen model is generally higher than that of the baseline model. During the compression stroke, which is in the range of 180 to 0 before top dead center (BTDC), the cylinder temperatures of both models rise gradually. After 10 CAD BTDC, which is the timing of spark ignition, both models experience dramatic increments of cylinder temperature. This is caused by the rapid combustion of fuels in a short period of time (30 CAD). It can be easily seen that the gradient of the baseline model's curve is lower than the gradient of the oxyhydrogen model's curve, which shows a higher combustion speed of hydrogen than the 4-MIX fuel (petrol and oil mixture). The baseline model reaches its maximum cylinder temperature of 3055.76 K at 19 CAD. However, the oxyhydrogen model reaches its maximum cylinder temperature of 2177.5 K at the same crank angle. And at the beginning of the exhaust stroke, which is at 180 CAD after top dead center (ATDC), the exhaust temperature of the oxyhydrogen model is 1882.69 K, while the exhaust cylinder temperature of the baseline model is much lower (969 K). The much-higher cylinder temperature of the oxyhydrogen model is due to the high flame temperature of hydrogen (around 3000 K under pure oxygen conditions and around 2300 K under standard air conditions) [6]. The compression of the oxygen–hydrogen mixture also intensifies the combustion process, so the maximum cylinder temperature obtained was 3056 K.

Figure 10b presents variations of cylinder pressure versus varying CAD for both models. The curves of both models coincides for the most part. The main difference is located where both curves reach their peaks. Unlike their cylinder temperature, both

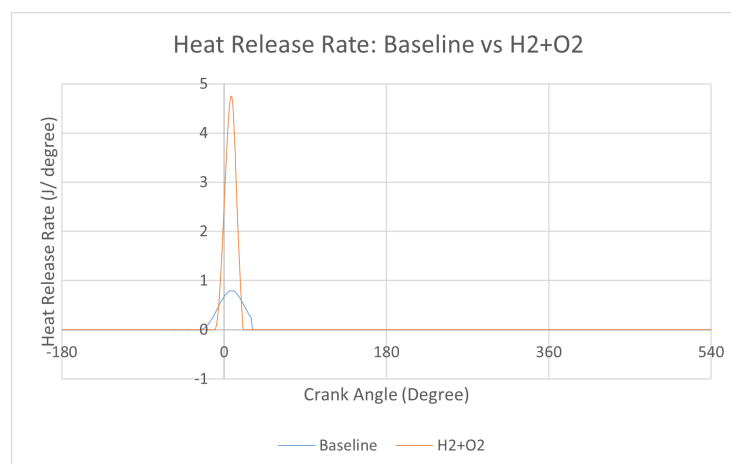
curves of cylinder pressure reach their maximums at different CAD. The cylinder pressure of the oxyhydrogen model reaches its maximum of 46.21 Bar at 10 CAD. However, the baseline model comes to the top of its cylinder pressure 5 CAD later than the model and its maximum value is slightly lower as well (43.92 kW). The compression ratio of the models was unchanged, at 9.8. Thus, only minor differences in peak pressure values and timings were observed.



(a)



(b)



(c)

Figure 10. Baseline model vs. oxyhydrogen models: temperature and pressure comparisons. (a) Cylinder temperature. (b) Cylinder pressure. (c) Heat release rate.

Figure 10c presents variations of the heat release rate versus carrying CAD for both models. After the timing of ignition, which is at 10 CAD BTDC, a significant difference can be seen between the models. The baseline model reaches its peak of 0.8 J/degree at 9 CAD ATDC and the oxyhydrogen model reaches its peak of 4.75 J/degree at 7.84 CAD ATDC. The figure shows the baseline and oxyhydrogen models' difference in heating value visually.

3.2.3. Discussion

There is no doubt that the application of the pure oxygen combustion technique solved the most essential problem very effectively—the emission of unwanted gases. By using hydrogen instead of fossil fuel and using pure oxygen instead of air, unwanted emission including nitrogen and carbon compounds can be eliminated theoretically. But on the other hand, this technique also triggered a significant drawback, which is the abnormally high cylinder temperature. In most realistic working occasions, engine materials cannot bear such high cylinder temperatures lasting for the whole compression stroke (0–180 CAD ATDC). However, the exhaust temperature of the pure oxygen combustion model was too high as well (1882.69 K at 180 CAD ATDC). Also, due to the high heat value and low density of hydrogen, the mass of contents injected into the engine cycle was significantly reduced. This reduction in the mass injected into the cylinder lowered thermal efficiency of the system. Thus, further improvements are required to solve these newly discovered drawbacks.

3.3. Water Injection Application

There were two main purposes for applying the water injection :

- (1) To reduce the general cylinder temperature and the exhaust gas; temperature
- (2) To keep the total injected mass constant.

The determination of required injection rate of fuel, pure oxygen, and water were shown in Section 2.6.

All simulations were carried out at the rated rotational speed of 7500 rpm, as it was determined that errors of energy input were nearly 0 at this speed in Section 3.2.1.

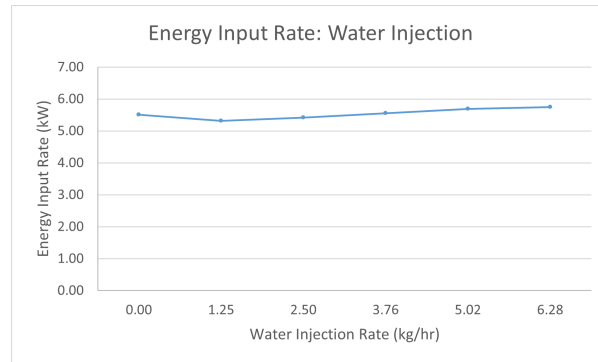
3.3.1. Performance Analysis

Figure 11 presents the performance results for varying rates of water injection at a constant rotational speed of 7500 rpm.

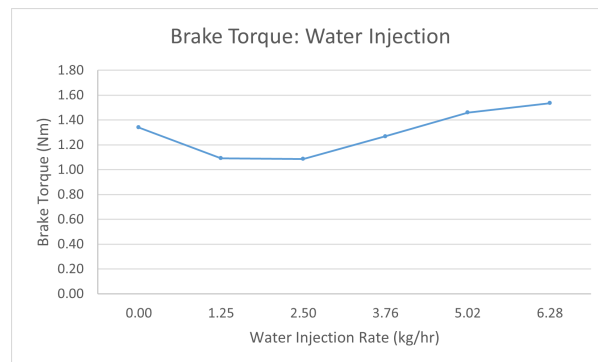
Figure 11a shows how the rate of water injection affects the rate of energy input. It can be easily seen that the rate of energy input is approximately kept at a stable level.

Figure 11b presents the variation of brake torque versus the water injection rate. The brake torque decreases as the water injection rate increases when the rate of water injection is no more than 2.5 kg/h. After this turning point of 2.5 kg/h, the curve starts to grow as the rate of water injection increases. The percentage changes in brake torque are larger than the rates of energy input, but the turning point at 2.5 kg/h can be seen in both Figure 11a,b.

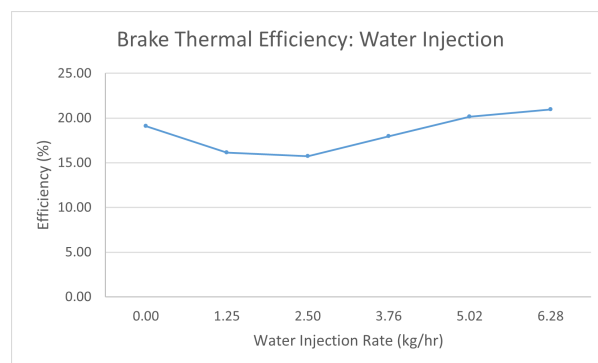
Figure 11c shows the variation of the brake thermal efficiency versus the rate of water injection. It shows a similar shape to the previous curves. The curve shows a decreasing–increasing trend with the point of turning located at 2.50 kg/h. Before this turning point, the brake power drops as the rate of water injection increases. Then, it starts to increase until it eventually climbs to its maximum point of 1.21 kW with 6.28 kg/h of water injection. When compared to the baseline model, the brake thermal efficiencies were generally lowered when the technique of water injection was applied. But after the rate of water injection was raised above 5.02 kg/h, the brake thermal efficiency could be improved to a level higher than the baseline model's.



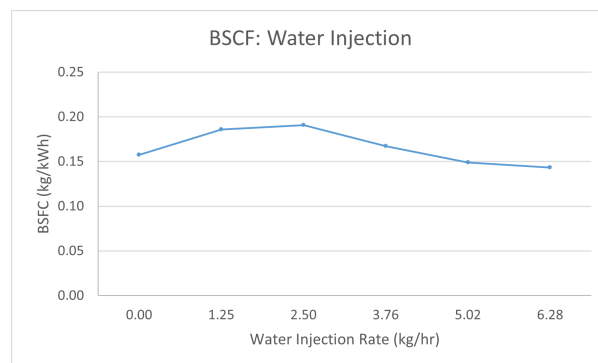
(a)



(b)



(c)



(d)

Figure 11. Water injection: engine performance analysis. (a) Energy input, (b) brake power, (c) brake thermal efficiency, (d) brake specific fuel consumption.

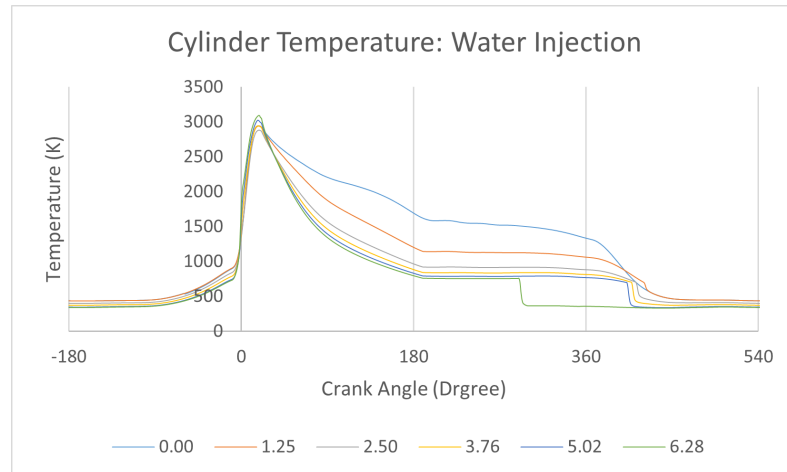
Figure 11d illustrates the change in BSFC versus the water injection rate. It shows an opposite trend to the previous curves. The curve of BSFC begins from 0.16 kg/h without any water injection and starts to rise until reaching its peak value of 0.19 kg/h. Then, it starts to decline until it reaches a lower level, which was 0.2 kg/h lower than the original value of BSFC. The variation of BSFC shows a strong correlation with the variations of brake thermal efficiency, since the engine operating in lower efficiency requires a higher rate of fuel consumption.

3.3.2. Pressure and Temperature Analysis

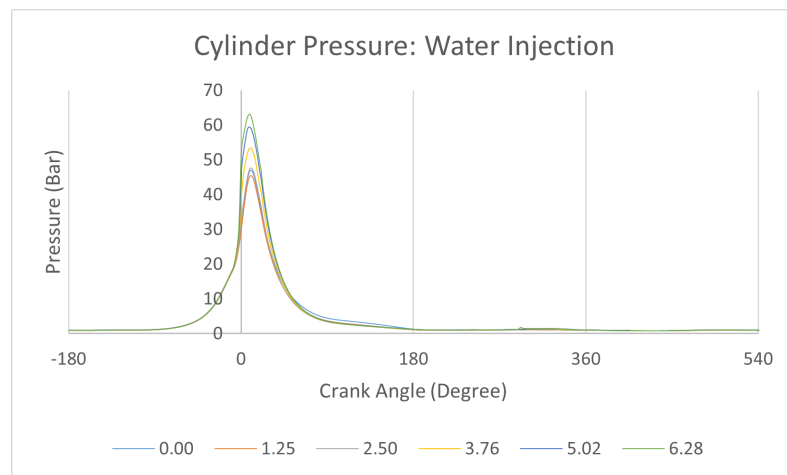
Figure 12 shows variations of cylinder pressure and cylinder temperature. Water injection seems very effective in terms of cylinder temperature reduction. While no water is injected into the combustion chamber, which is the original situation shown in Section 3.2, the peak temperature is 3243 K, and the exhaust temperature is 1977 K. While the water injection rate is increased from 0 to 2.5 kg/h, the technique shows dramatic influences on exhaust temperature. The effectiveness can be easily seen from two large gaps between the curves of 0 kg/h and 2.5 kg/h. This can be explained by the strong heat absorption ability of water during the gasification process. After that, the increment of the water injection rate keeps reducing the cylinder temperature to a minor extent, but not as strong as previously anymore. When it comes to the peak temperature, although the peak cylinder temperatures are all above 2800 K no matter how great a rate of water is injected into the chamber, water injection triggers a constant reduction in cylinder temperature after the point of peak temperature, which aims to control the cylinder temperature into a bearable temperature range. Because water was directly injected into the model after the combustion was nearly finished, the combustion environment inside the combustion chamber until the theoretical peak point was never changed; thus, the peak combustion temperature was not affected. But after the peak point, gasification of liquid water to vapour starts to take heat from charges; thus, the cylinder temperature then starts to decrease.

3.3.3. Discussion

It can be concluded that the effect of water injection depends on its rate. With a low water injection volume, water injection may produce negative effects on engine performances. But after the amount of water injection is raised over a certain value, positive effects of engine performance start to show up. The turning point can be roughly located at a water injection rate of around 2.5 kg/h. When the rate of water injection is lower than 2.5 kg/h, water injection can barely help with any engine performance characteristic. But after the rate of water injection increases over 2.5 kg/h, the technique starts to give improvements in engine performance. When 2.5 kg/h of water is injected into the combustion chamber, the exceeding cylinder temperature can be reduced to an acceptable level (<2000 K) in 28 CAD, which is 0.224 s in every cycle. Such a short time of exceeding cylinder temperature can be neglected and will not produce any hazards towards the safe operation of the engine. Overall, a water injection rate of 2.5 kg/h can be regarded as a point that meets halfway between engine performance and cylinder temperature management. This rate of water injection will therefore be used in the next model.



(a)



(b)

Figure 12. Water injection models: temperature and pressure comparisons. (a) Cylinder temperature. (b) Cylinder pressure.

3.4. EIVC Miller Cycle Application

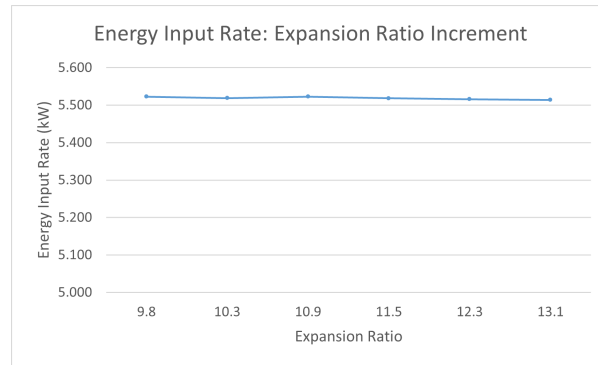
The main purpose of this group of simulations is to investigate the effectiveness of Miller cycle application, more precisely, the early-intake valve closure technique. The extent of early-intake valve closure was increased from 0% to 25% while the compression ratio was kept unchanged at 9.8. Thus, the expansion ratio was increased from 9.8 to 13.1.

All simulations were carried out at the rated rotational speed of 7500 rpm, and the rate of water injection in this EIVC Miller cycle model was set at 3 kg/h. That is possibly due to the application of high expansion ratio and EIVC enhancing the water gasification effect, which thus hinders the fuel combustion process at a high water injection rate. The results are presented in the following sub-sections.

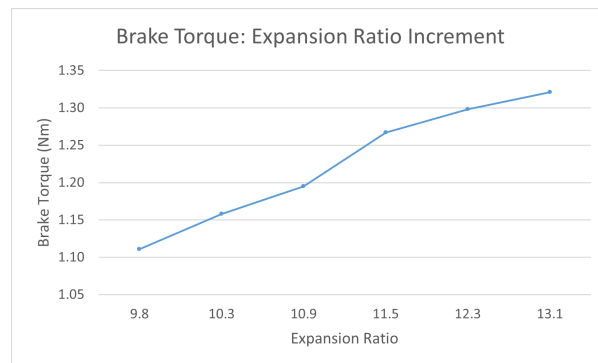
3.4.1. Performance Analysis

Figure 13 shows the performance results of the EIVC Miller cycle model with rising extents of early-intake valve closure.

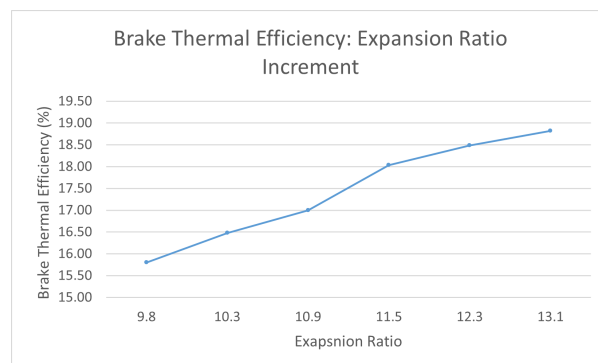
Figure 13a presents the energy input results for varying expansion ratios. It is very apparent that the rate of energy input was kept in a stable range of 5.51–5.52 kW.



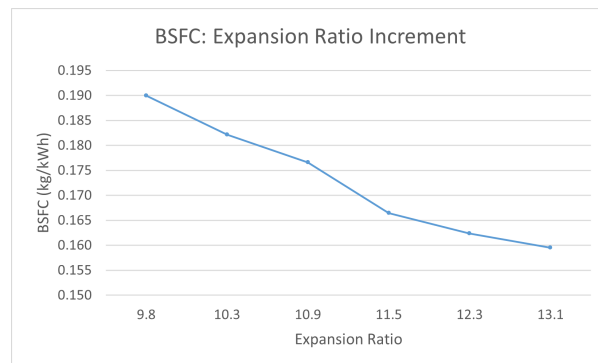
(a)



(b)



(c)



(d)

Figure 13. Early-intake valve closure Miller cycle: engine performance analysis. (a) Energy input, (b) brake power, (c) brake thermal efficiency, (d) brake specific fuel consumption.

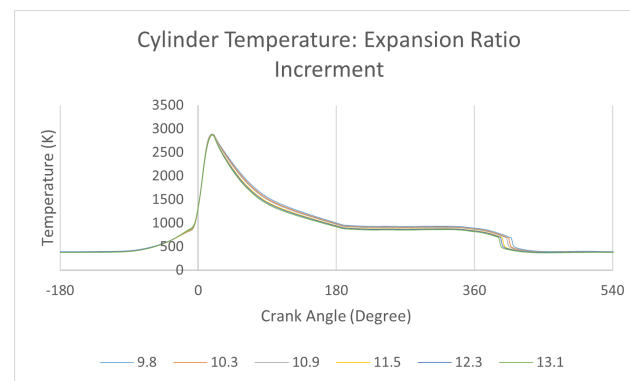
Figure 13b shows the variation of brake torque versus varying expansion ratio. Generally, it shows an increasing trend with all positive but fluctuating gradients. The curve starts from 1.11 Nm under the 0% early-intake valve closure condition, then it experiences a steady increment until its value reaches 1.19 Nm under the 10% early-intake valve closure condition. After that, the curve encounters a rapid increment of 0.08 Nm when the extent of early-intake valve closure is increased from 10% to 15%. Eventually, another steady increment can be observed when the extent of early-intake valve closure is increased from 15% to 25%. The curve shows the highest rate of increment between expansion ratios of 10.9 and 11.5, when 6.01% of brake torque is raised.

Figure 13c presents the variation of the brake thermal efficiency versus varying expansion ratio. Interestingly, the curve shows a very similar trend to the curve of brake torque. This phenomenon can be visually seen from comparing the values of percentage change in Figure 13b,c. This phenomenon can be explained by the linear relationship between brake thermal efficiency and brake torque when the values of energy input are fixed at a stable level.

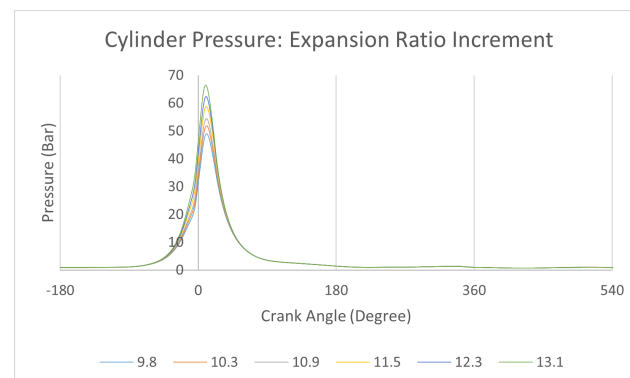
Figure 13d illustrates the change in BSFC versus varying expansion ratio. Overall, it shows a reversely proportional trend that decreases as the extent of early-intake valve closure increases. Eventually, the BSFC of the model is reduced to 83.68% of its original value.

3.4.2. Temperature and Pressure Analysis

As shown in Figure 14a,b, the increment of early-intake valve closure and expansion ratio does not produce strong effects on cylinder temperature because of the unchanged fuel input rate and sufficient supply of oxidizer at all times. The maximum cylinder pressure increases by 35.86% comparing to its original value of 46.97 bar.



(a)



(b)

Figure 14. Early Intake Valve closure: engine performance analysis. (a) Cylinder temperature, (b) cylinder pressure.

3.4.3. Discussion

Based on the performance results of all engines depicted in Figure 13, a general rule can be inferred: engine performance parameters, including brake torque, brake thermal efficiency, and BSFC, show improvements as the percentages of valve opening profiles are reduced. The EIVC technique does not significantly affect cylinder temperature, but it notably increases cylinder pressure.

3.5. Overall Results Comparisons

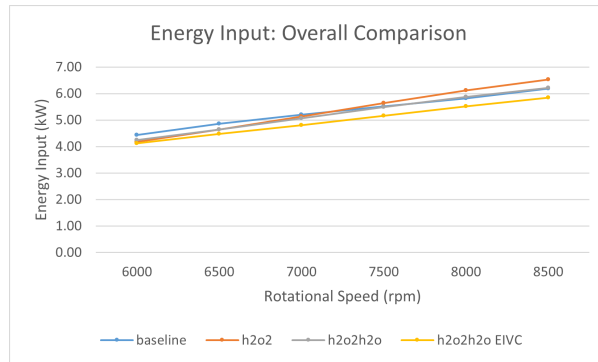
All key parameters and the best results of all models are concluded and listed in Table 1.

Table 1. Best results of each model.

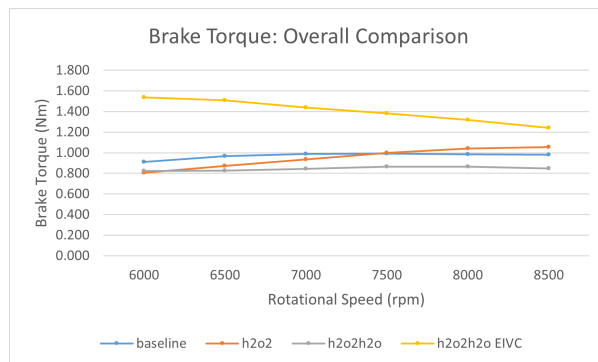
Parameters	4-MIX	Baseline	Oxyhydrogen	Water Injection	EIVC
Rotational Speed (rpm)	7500.0	7500.0	7500.0	7500	7500
Energy Input Rate (kW)	5.52	5.51	5.64	5.55	5.52
Brake Power (kW)	1.000	0.993	0.999	0.996	1.036
Brake Torque (Nm)	1.27	1.26	1.27	1.53	1.32
Brake Thermal Efficiency (%)	18.1	18.0	17.7	21.0	18.8
BSFC (g/kWh)	480.0	499.9	169.6	143.1	165.6
HC Emission (g/kWh)	-	17.9	0.0	0.0	0.0
NOx Emission (g/kWh)	-	0.4	0.0	0.0	0.0
HC+NOx Emission (g/kWh)	18.0	18.3	0.0	0.0	0.0
Max. Cylinder Temperature (K)	-	2177.5	3055.8	3093.8	2876.5
Exhaust Temperature (K)	-	969.1	1890.8	796.0	918.5
Max. Cylinder Pressure (Bar)	-	43.9	46.2	63.3	66.53
Water Injection Rate (kg/h)	0.0	0.0	0.0	6.3	2.5
EIVC (%)	0.0	0.0	0.0	0.0	25.0
Compression Ratio	9.8	9.8	9.8	9.8	9.8
Expansion Ratio	9.8	9.8	9.8	9.8	13.1

Figure 15a presents all models' varying energy input rate versus changes in rotational speeds. Overall, all models show smooth increasing trends with minor differences. The EIVC model consumes fuel at the lowest rate among all models at all rotational speeds. After that, as the rotational speed increases, the energy input rates of all models go up in different gradients. When the rotational speed is around 7300 rpm, the energy input rates of all models except the EIVC model overlap at 5.4 kW. Generally, the EIVC model consumes 93.41% of the input energy of the baseline model on average.

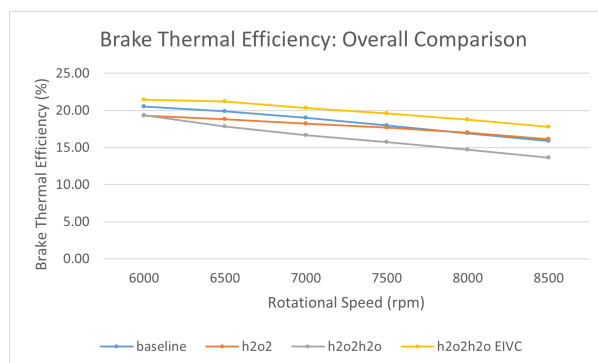
Figure 15b shows the variation of brake torque versus the rotational speed of all models' best results. Overall, the curve of the oxyhydrogen model presents an increasing trend and the curve of the EIVC model presents a decreasing trend. The curves of the baseline model and the water injection model show partial parabolic shapes. It is very apparent that the EIVC model's data curve stays in the highest place among all models at all rotational speeds. And on the other hand, the water injection model's curve stays in the lowest position among all models at all rotational speeds except 6000 rpm. At a rotational speed of 6000 rpm, the brake torque of the oxyhydrogen produces 0.806 Nm of torque, which is even slightly lower than the water injection model. At the rated rotational speed of 7500 rpm, the baseline model and the oxyhydrogen model overlap at the point around 0.996 Nm. At the same moment, the brake torque produced by the EIVC model is 38.65% higher than the overlapped value and the brake torque produced by the water injection model is 13.4% lower than the overlapped value.



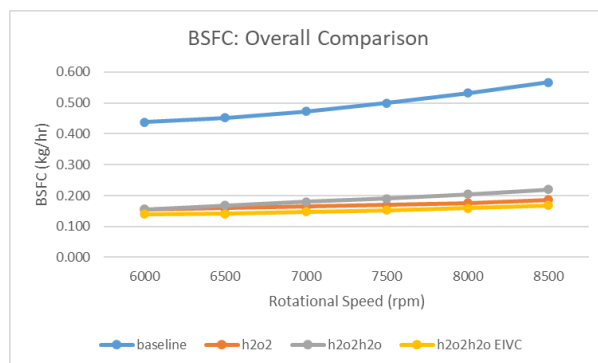
(a)



(b)



(c)



(d)

Figure 15. Combined comparisons: (a) energy input, (b) brake torque, (c) brake thermal efficiency, (d) brake specific fuel consumption.

Figure 15c illustrates changes in the brake thermal efficiency of all models at different rotational speeds. Still, the line of the EIVC model stays at the top among all models and eventually, it receives an improvement of 4.58% compared to the baseline model at a rotational speed of 8500 rpm. The line of the water injection model and the line of the oxyhydrogen combustion model start from the same point of around 19.3% brake thermal efficiency at a rotational speed of 6000 rpm. And after that, the difference between their values rises as the rotational speed increases. The line of the baseline model and the line of the oxyhydrogen model have a difference of 1.19% at the beginning of 6000 rpm. And then they start to approach each other as the rotational speed goes up. Finally, at a rotational speed of 8500 rpm, the baseline and oxyhydrogen models produce similar levels of brake thermal efficiency (around 16%).

Figure 15d shows the brake specific fuel consumption of all four models versus the increment of rotational speed. All models' BSFCs gradually increase with the increment of rotational speed. Obviously, the baseline model burns fuel in the highest rate; it can be seen from the figure that the curve of the baseline model stands above those of the remaining three models, with a clear gap in between. This can be explained by the high heating value of hydrogen, as it can release thermal energy at a much higher rate than the mixture of petrol and oil (50:1).

4. Conclusions

In this study, a modified spark ignition oxyhydrogen-fuelled internal combustion engine Miller cycle with water injection application was proposed and simulated.

The main structure of the baseline model makes reference to an existing petrol-fuelled engine—Stihl 4-MIX 31cc. The layout principle of the simulation model refers to Li's study [17], with upgrades and refinements in the combustion and friction submodels. The results for brake power, brake specific consumption, and emissions were compared with the experimental results given by Knaus et al. for validation and calibration [22]. They show that all simulation errors can be controlled in an acceptable range that is below 5%. And the simulation model shows its highest accuracy at a rotational speed of 7500 rpm, which is exactly the 4-MIX engine's optimal rated working load. Thus, it is proved that the simulation model illustrates its accuracy of prediction in terms of engine performance and emission.

The oxyhydrogen model was modified based on the baseline model. In principle, the previous petrol-fuelled engine model was altered in terms of fuels, from a fossil fuel, petrol, into a renewable fuel, hydrogen. Also, the carrying fluid, air, was replaced with pure oxygen for the complete removal of the nitrogen and carbon elements contained in air. The replacement of fuels and carrying fluid aimed to eliminate emissions that are toxic to the environment (CO_2 , NO , NO_2) and provide a potential source of water for the application of water injection. At the same energy input rate, the results of engine performance (brake torque, thermal efficiency, and BSFC) were compared with the baseline model's. Both the baseline and oxyhydrogen model show descending trends, while the baseline model's is relatively steeper, and the oxyhydrogen model's is quite flat. At a rotational speed of 7500 rpm, which is the rated working load, both models produce a brake torque of 1.24 Nm. As for the brake thermal efficiency, the oxyhydrogen model's results are generally lower than the baseline model's, with an upper limit of 20% and a lower limit of 16%. When it comes to BSFC, a significant difference can be seen from the results. The BSFC of the oxyhydrogen model is around three times as much as the baseline's. This can be explained by the fuels' differences in heating value, as was mentioned in Section 2.1. The cylinder temperature of the oxyhydrogen model is much higher than the baseline model's, as well as the rate of temperature increment, since the flame temperature and speed of hydrogen are much higher than petrol's.

The application of water injection aimed to not only reduce cylinder temperature, but also keep the mass input constant, since hydrogen is a fuel with a lower density but higher heating value than petrol. An additional water injector was attached to the oxyhydrogen

model. The rate of water injection was calculated based on the principle of mass input constant. The rate of water injection was tried from 0 kg/h as the non-water injection condition to 6.28 kg/h as the exceeding mass input condition. Among all the results, including engine performance, cylinder pressure, and cylinder temperature, it was found that a water injection rate of 2.5 kg/h could be regraded as a turning point. When the rate of water injection was lower than 2.5 kg/h, increasing the rate of water injection produced negative effects toward engine performance but apparently positive effects toward cylinder pressure and cylinder temperature. Thus, the water injection rate of 2.5 kg/h was selected as meeting the halfway point between solving the hazard of excessive cylinder temperature and keeping the engine's performance in an acceptable range.

When it comes the the model with Miller cycle application, based on the modification made in the water injection model with a water injection rate of 2.5 kg/h, the expansion ratio was increased from 9.8 in the baseline condition to 13.1 at maximum. Generally, a trend can be concluded that the increment of expansion ratio can produce positive effects towards engine performance. However, it does not produce noticeable effects on the combustion process and results while significantly raise the cylinder pressure.

In summary, the EIVC Miller cycle exhibited superior performance in terms of energy efficiency, torque output, and thermal efficiency compared to alternative models, effectively addressing concerns related to emissions and cylinder temperatures.

As for other progressive studies in potential, the problem of exceeding the cylinder temperature caused by hydrogen combustion can also possibly be solved by noble gas dilution. Due to noble gases' characteristics of nonreactivity, the exhausted noble gas can be isolated from the mixture by condensation and then recycled for reuse. At the same time, the byproduct of condensed water can be used for the application of water injection as well. Possible drawbacks may include the accurate determination of mixing ratio and the occupation of space when it comes to commercial engine application. This novel principle based on the current results shown in this study will be further investigated in the future.

Author Contributions: Conceptualization, Y.W.; Methodology, X.K.; Software, X.K.; Formal analysis, Y.W.; Investigation, X.K.; Data curation, X.K.; Writing—original draft, X.K.; Writing—review & editing, X.K.; Supervision, Y.W.; Project administration, Y.W. All authors have read and agreed to the published version of the manuscript.

Funding: This research received no external funding.

Data Availability Statement: All data are in the paper.

Conflicts of Interest: The authors declare no conflict of interest.

Abbreviations

The following abbreviations are used in this report:

ATDC	After Top Dead Center
BSFC	Brake Specific Fuel Consumption
BTDC	Before Top Dead Center
CAD	Crank Angle Degree
CI	Compression Ignition
EIVC	Early-Intake Valve Closure
HC	Unburned Hydrocarbon
ICE	Internal Combustion Engine
LIVC	Late-Intake Valve Closure
NO _x	Sum of Nitric Oxide (NO) and Nitrogen Dioxide (NO ₂)
O ₂ + H ₂	Oxyhydrogen
RPM	Rotations per Minute
SI	Spark Ignition
VVL	Variable Valve Lift
VVT	Variable Valve Timing

Appendix A. Valve Opening Profile—MATLAB Code

```

clc;
clear all;

x_ex = 70: 1: 430;
%original exhaust valve opening duration, fixed

y = normpdf(x_ex, 250, 57);
%normal distribution with 250 as mu and 57 as sigma
y_max = max(y);
%peak value of the curve
y_ex_times = 3.2 / y_max;
%ratio of standard normal distribution peak value to
%the maximum valve lift of exhaust valve
y_ex = y .* y_ex_times;
%y value of exhaust valve, fixed

shrink_ratio = 0.75;
%percentage of valve opening

x_in = 300: shrink_ratio: 300+shrink_ratio*360;
%x values of intake valve
y_in_times = 3.2 * shrink_ratio / y_max;
%ratio of standard normal distribution peak value to
%the maximum valve lift of exhaust valve
y_in = y .* y_in_times;
%y values of intake valve

figure;
hold on;
plot(x_ex, y_ex);
plot(x_in, y_in);

xlim = ([50 450]);
ylim = ([0 3.5]);

```

Appendix B. WAVE Settings—Intake Ducts

Table A1. Realis WAVE settings—intake ducts.

Condition	Input	Unit
Left Diameter	50	mm
Right Diameter	30	mm
Overall Length	50	mm
Discretization Length	16	mm
Wall Friction	1	-
Wall Heat Transfer	1	-
Wall Temperature	300	K
Fluid State	Intake Fluid State	-
Fluid Composition	Fluid Composition—Air	-
(a) Duct 1		
Condition	Input	Unit
Left Diameter	30	mm
Right Diameter	15	mm
Overall Length	50	mm
Discretization Length	16	mm
Wall Friction	1	-
Wall Heat Transfer	1	-
Wall Temperature	300	K
Fluid State	Intake Fluid State	-
Fluid Composition	Fluid Composition—Air	-
(b) Duct 2		

Table A1. *Cont.*

Condition	Input	Unit
Left Diameter	15	mm
Right Diameter	15	mm
Overall Length	30	mm
Discretization Length	18	mm
Wall Friction	1	-
Wall Heat Transfer	1	-
Wall Temperature	300	K
Fluid State	Intake Fluid State	-
Fluid Composition	Fluid Composition—Air	-
(c) Duct 3		

Appendix C. Realis WAVE Settings—Ambients**Table A2.** Realis WAVE settings—ambients.

Condition	Input	Unit
Fluid State	Intake Fluid State	-
Fluid Composition	Fluid Composition—Air	-
(a) Intake		
Condition	Input	Unit
Fluid State	Exhaust Fluid State	-
Fluid Composition	Fluid Composition—Air	-
(b) Exhaust		

Appendix D. Realis WAVE Settings—Exhaust Ducts**Table A3.** Realis WAVE settings—exhaust ducts.

Condition	Input	Unit
Left Diameter	15	mm
Right Diameter	30	mm
Overall Length	50	mm
Discretization Length	22	mm
Wall Friction	1	-
Wall Heat Transfer	1	-
Wall Temperature	400	K
Fluid State	Exhaust Fluid State	-
Fluid Composition	Fluid Composition—Air	-
(a) Duct 4		
Condition	Input	Unit
Left Diameter	30	mm
Right Diameter	50	mm
Overall Length	50	mm
Discretization Length	22	mm
Wall Friction	1	-
Wall Heat Transfer	1	-
Wall Temperature	400	K
Fluid State	Exhaust Fluid State	-
Fluid Composition	Fluid Composition—Air	-
(b) Duct 5		

Appendix E. Realis WAVE Settings—Cyl1

Table A4. Realis WAVE settings—Cyl1.

Condition	Input	Unit
Bore	40	mm
Crank Stroke	25	mm
Clearance Height	1	-
Heat Area Multiplier	1	-
Piston Area Multiplier	1	-
Connecting Rod Length	13	mm
Pin Offset	0	mm
Compression Ratio	9.8	-
Piston	520	K
Liner	400	K
Head	520	K
Intake Valve	420	K
Exhaust Valve	480	K
Swirl Ratio	0	-
Fluid State	Intake Fluid State	-
Submodel—Type	Two Zones	-
Submodel—Combustion	Multi-Wiebe Combustion	-
Heat Transfer	Woschni Heat Transfer Model	-

Appendix F. Realis WAVE Settings—Crankcase

Table A5. Realis WAVE settings—crankcase.

Condition	Input	Unit
Compression Ratio	2	-
Piston Underside	350	K
CrankCase Wall	350	K
Cylinder Liner	350	K
Intake Valve	400	K
Exhaust Valve	450	K
Swirl Ratio	0	-
Fluid Compression	Fluid Composition—Air	-
Submodel—Heat Transfer	Woschni Heat Transfer Model	-

Appendix G. Realis WAVE Settings—Fluid States

Table A6. Realis WAVE settings—fluid states.

Condition	Input	Unit
Pressure	1	Bar
Temperature	300	K
Initial Velocity	0	ms ⁻¹
(a) Fluid State—Intake		
Condition	Input	Unit
Pressure	1.05	Bar
Temperature	900	K
Initial Velocity	0	ms ⁻¹
(b) Fluid State—Exhaust		

Appendix H. Realis WAVE Settings—Engine block

Table A7. Realis WAVE settings—engine block.

Condition	Input	Unit
Engine Shape	Inline	-
Mixture Type	Homogeneous (SI)	-
Stroke Per Cycle	4	-
Engine Speed	6000–8500	RPM
Reference Temperature	298	K
Reference Pressure	1	Bar
Engine Friction	Chen–Flynn Friction Model	-
Scavenging	Scavenging Model	-

Appendix I. Realis WAVE Settings—Valves

Table A8. Realis WAVE settings—valves.

Condition	Input	Unit
Valve Type	Orifice	-
Reference Diameter	14.5	mm
(a) Valve 1		
Condition	Input	Unit
Valve Type	Orifice	-
Reference Diameter	14.5	mm
(b) Valve 2		
Condition	Input	Unit
Valve Type	Lift	-
Reference Diameter	14.5	mm
Reference Diameter	14.5	mm
Geometric Diameter	14.5	mm
Lift Profile	Intake Valve Lift	-
Flow Coefficient Profile	Valve Flow Coefficient Profile	-
(c) Valve 3		
Condition	Input	Unit
Valve Type	Lift	-
Reference Diameter	14.5	mm
Reference Diameter	14.5	mm
Geometric Diameter	14.5	mm
Lift Profile	Exhaust Valve Lift	-
Flow Coefficient Profile	Valve Flow Coefficient Profile	-
(d) Valve 4		
Condition	Input	Unit
Coefficient Type	Flow Coefficient	-
Profile Type	Forward/Reverse	-
Specified by	Tag (predefined profile)	mm
Tag	Typical Valve Flow Coefficient Profile (CFTYP)	-
(e) Valve Flow Coefficient Profile		

Appendix J. Realis WAVE Settings—Model Properties

Table A9. Realis WAVE settings—model properties.

Condition	Input	Unit
Compressibility	Ideal Gas	-
Calculation Method	Interpolation	-
Wall Friction	1	-
Heat Transfer	1	-
Acceleration	9.8	ms ⁻²
Specify by	Vector	-
X	0	-
Y	0	-
Z	-1	-
NO Molecular Weight	30	gmol ⁻¹
CO Molecular Weight	28	gmol ⁻¹

Appendix K. Realis WAVE Settings—Fluid Compositions

Table A10. Realis WAVE settings—fluid compositions.

Condition	Input	Unit
Fresh Air	1	-
Burned Air	0	-
Vaporized Fuel	0	-
Burned Fuel	0	-
Liquid Fuel	0	-
(a) Fluid Composition—Air		
Condition	Input	Unit
Fresh Air	0	-
Burned Air	0	-
Vaporized Fuel	0	-
Burned Fuel	0	-
Liquid Fuel	1	-
(b) Fluid Composition—Liquid Fuel		
Condition	Input	Unit
Fresh Air	0	-
Burned Air	0	-
Vaporized Fuel	1	-
Burned Fuel	0	-
Liquid Fuel	0	-
(c) Fluid Composition—Gaseous Fuel		

Appendix L. Realis WAVE Settings—Submodels

Table A11. Realis WAVE settings—submodels.

Condition	Input	Unit
Model Type	Original Woschni	-
Intake Valve Open	1	-
Intake Valve Closed	1	-
(a) Woschni Heat Transfer Model		
Condition	Input	Unit
Curve Fit Type	1-point Curve	-
First Point—Cumulative Burn Fraction	0.1	-
Second Point—Cumulative Burn Fraction	0.5	-
Second Point—Crank Position	8	CAD
Third Point—Cumulative Burn Fraction	0.9	-
Combustion Duration	18	CAD
Wiebe Exponent	2	-
Mass Ratio	1	-
Profile Control	Terminate at	-
Burn Fraction at Completion	0.96	-
(b) Multi-Wiebe Combustion Model		
Condition	Input	Unit
Profile	Fully	-
Temperature Threshold	0	-
(c) Scavenging Model		

Appendix M. Realis WAVE Settings—Fuel Files

Table A12. Realis WAVE settings—fuel files.

Condition	Input	Unit
Carbon	8	-
Hydrogen	18	-
Oxygen	0	-
Nitrogen	0	-
Entropy of Formation	-3487.78	Jkg ⁻¹ K ⁻¹
Lower Heating Value	43 × 10 ⁶	Jkg ⁻¹
Density	702.67	kgm ³
Specific Heat	2202	Jkg ⁻¹ K ⁻¹
Heat of Vaporization	-0.362 × 10 ⁶	Jkg ⁻¹
(a) 4-MIX Fuel File		
Condition	Input	Unit
Carbon	0	-
Hydrogen	2	-
Oxygen	1	-
Nitrogen	0	-
Entropy of Formation	-2492.94	Jkg ⁻¹ K ⁻¹
Lower Heating Value	0	Jkg ⁻¹
Density	1000.00	kgm ³
Specific Heat	4176	Jkg ⁻¹ K ⁻¹
Heat of Vaporization	-2.4 × 10 ⁶	Jkg ⁻¹
(b) Water Fuel File		

Appendix N. Realis WAVE Settings—Injectors

Table A13. Realis WAVE settings—fuel injectors.

Condition	Input	Unit
Injector Type	Mass Flow Rate	-
Fuel Type	Water	-
Start of Injection	19	CAD
Mixture Temperature	300	K
Nozzle Diameter	0.2	mm
Number of Holes	8	-
Mean Fuel Drop Diameter	AUTO	-
Injector Sac Volume	0	mm ³
Spray Spread Angle	40	Degree
Initial Fuel Injector Velocity	Calculate Automatically	-
Fuel Composition	Fluid Composition—Liquid Fuel	-
(a) Water Injector		
Condition	Input	Unit
Injector Type	Proportional	-
Fuel Type	4-MIX Fuel; Hydrogen; Hydrogen; Hydrogen	-
Fuel/Air Ratio	0.0833; 0.0526; 0.0526; 0.0385	-
Mixture Temperature	300	K
Nozzle Diameter	0.2	mm
Number of Holes	8	-
Mean Fuel Drop Diameter	AUTO	-
Evaporated Liquid Fraction	Scavenging Model	-
Spray Spread Angle	40	Degree
Initial Fuel Injector Velocity	Carburetor	-
Fuel Composition	Fluid Composition—Liquid Fuel; Gaseous Fuel; Gaseous Fuel; Gaseous Fuel	-
(b) 4-MIX Fuel File		

References

- Teoh, Y.H.; How, H.G.; Le, T.D.; Nguyen, H.T.; Loo, D.L.; Rashid, T.; Sher, F. A review on production and implementation of hydrogen as a green fuel in internal combustion engines. *Fuel* **2023**, *333*, 126525. [CrossRef]
- BP. *Statistical Review of World Energy 2022*; BP: London, UK, 2023.
- Asghar, U.; Rafiq, S.; Anwar, A.; Iqbal, T.; Ahmed, A.; Jamil, F.; Khurram, M.S.; Akbar, M.M.; Farooq, A.; Shah, N.S.; et al. Review on the progress in emission control technologies for the abatement of CO₂, SO_x and NO_x from fuel combustion. *J. Environ. Chem. Eng.* **2021**, *9*, 106064. [CrossRef]
- Horowitz, C.A. Paris agreement. *Int. Leg. Mater.* **2016**, *55*, 740–755. [CrossRef]
- The World Bank, Climate Watch Historical GHG Emissions (1990–2020). World Resources Institute: Washington, DC, USA, 2023. Available online: https://www.climatewatchdata.org/ghg-emissions?end_year=2020&start_year=1990 (accessed on 1 April 2024).
- Heywood, J.B. *Internal Combustion Engine Fundamentals*; McGraw-Hill Education: New York, NY, USA, 2018.
- Korakianitis, T.; Namasivayam, A.; Crookes, R. Natural-gas fueled spark-ignition (SI) and compression-ignition (CI) engine performance and emissions. *Prog. Energy Combust. Sci.* **2011**, *37*, 89–112. [CrossRef]
- Wind, J. Hydrogen-fueled road automobiles—Passenger cars and buses. In *Compendium of Hydrogen Energy*; Elsevier: Amsterdam, The Netherlands, 2016; pp. 3–21.
- Eckermann, E. *World History of the Automobile*; SAE International: Warrendale, PA, USA, 2001.
- Chute, R. Pressure compounding a four cycle diesel engine. *SAE Trans.* **1985**, *94*, 685–699.
- Zheng, B.; Yin, T.; Li, T. *Analysis of Thermal Efficiency Improvement of a Highly Boosted, High Compression Ratio, Direct-Injection Gasoline Engine with Livc and Eivc at Partial and Full Loads*; No. 2015-01-1882. SAE Technical Paper, SAE International: Detroit, MI, USA, 2015.
- Li, T.; Gao, Y.; Wang, J.; Chen, Z. The Miller cycle effects on improvement of fuel economy in a highly boosted, high compression ratio, direct-injection gasoline engine: EIVC vs. LIVC. *Energy Convers. Manag.* **2014**, *79*, 59–65. [CrossRef]

13. Zhu, S.; Hu, B.; Akehurst, S.; Copeland, C.; Lewis, A.; Yuan, H.; Kennedy, I.; Bernards, J.; Branney, C. A review of water injection applied on the internal combustion engine. *Energy Convers. Manag.* **2019**, *184*, 139–158. [[CrossRef](#)]
14. Xu, P.; Ji, C.; Wang, S.; Cong, X.; Ma, Z.; Tang, C.; Meng, H.; Shi, C. Effects of direct water injection on engine performance in engine fueled with hydrogen at varied excess air ratios and spark timing. *Fuel* **2020**, *269*, 117209. [[CrossRef](#)]
15. Fan, B.; Zeng, Y.; Zhang, Y.; Pan, J.; Yang, W.; Wang, Y. Research on the hydrogen injection strategy of a direct injection natural gas/hydrogen rotary engine considering apex seal leakage. *Int. J. Hydrogen Energy* **2021**, *46*, 9234–9251. [[CrossRef](#)]
16. Ran, Z.; Hariharan, D.; Lawler, B.; Mamalis, S. Experimental study of lean spark ignition combustion using gasoline, ethanol, natural gas, and syngas. *Fuel* **2019**, *235*, 530–537. [[CrossRef](#)]
17. Li, C. An Investigation of the Performance of a Free-Piston Engine Using Miller Cycle and Renewable Fuels. Doctoral Thesis, Durham University, Durham, UK, 2022.
18. Wu, C.; Puzinauskas, P.V.; Tsai, J.S. Performance analysis and optimization of a supercharged Miller cycle Otto engine. *Appl. Therm. Eng.* **2003**, *23*, 511–521. [[CrossRef](#)]
19. Zhao, J. Research and application of over-expansion cycle (Atkinson and Miller) engines—A review. *Appl. Energy* **2017**, *185*, 300–319. [[CrossRef](#)]
20. Clarke, D.; Smith, W.J. *The Simulation, Implementation and Analysis of the Miller Cycle Using an Inlet Control Rotary Valve*; SAE Technical Paper; SAE International: Warrendale, PA, USA, 1997.
21. Ji, C.; Hong, C.; Wang, S.; Xin, G.; Meng, H.; Yang, J.; Qiang, Y. Evaluation of the variable valve timing strategy in a direct-injection hydrogen engine with the Miller cycle under lean conditions. *Fuel* **2023**, *343*, 127932. [[CrossRef](#)]
22. Knaus, K.; Häberlein, J.; Becker, G.; Rosskamp, H. *A New High-Performance Four-Stroke Engine for All-Position Use in Hand-Held Power Tools*; SAE Technical Paper, No. 2004-32-0075; SAE International: Detroit, MI, USA, 2004.
23. *Ricardo Software*, Version 2020.3; WAVE User Manual; Ricardo Software Limited: Detroit, MI, USA, 2014.

Disclaimer/Publisher’s Note: The statements, opinions and data contained in all publications are solely those of the individual author(s) and contributor(s) and not of MDPI and/or the editor(s). MDPI and/or the editor(s) disclaim responsibility for any injury to people or property resulting from any ideas, methods, instructions or products referred to in the content.